Manual of Remote Sensing

Imaging Radar Interferometry

Søren N. Madsen and Howard A. Zebker

Jet Propulsion Laboratory

California Institute of Technology

1 introduction

1.1 Developments in SAR Interferometry

Synthetic aperture radar (SAR) has been used for high resolution imaging from aircraft and satellites for many years (see Volume 1, chapter 10, for a description of the technique and Curlander and McDonough [1991] for a more recent review). SAR interferometric techniques combine complex images recorded by antennas at different locations or at different times to form interferograms which permit the determination of minute differences in the range (distance) to corresponding points of an image pair, on the sub-wavelength scale. The feasibility of using an airborne SAR system in an interferometric mode to generate topographic contours was first demonstrated, using optical processing techniques, by Graham of Goodyear Aerospace Corporation, [Graham, 1974]. This system formed a sum signal interferometer from the signals received by two antennas mounted above each other on a single side-looking movable gimbal. These techniques were later refined at NASA's Jet Propulsion Laboratory [Zebker and Goldstein, 1986], who used digital processing techniques to implement a correlation interferometer. JPL also demonstrated this technique applied to satellite SAR data acquired on separate passes [Goldstein et rd., 1988], [Li and Goldstein, 1990]. A corresponding repeat track implementation using an aircraft platform was first reported by the Canada Centre for Remote Sensing [Gray and Farris-Manning, 1993]. A vexing problem in interferometry, that the phase of the interferograrn is only measured modulo 2π while it is the absolute value of the phase that is needed for analysis, was also addressed by Goldstein et at., who developed a technique to determine the absolute interferometric phase to within a constant. Using one known scene elevation they determined this constant and the elevations of all other image points could be estimated. By combining multiple interferograms Gabriel et al. [1989]

demonstrated that differential applications of interferometry can be used to detect and estimate very small (sub centimeter) surface perturbations.

In another development, a configuration of two antennas mounted along the fuselage of an aircraft in the direction of motion was shown to provide information on ocean surface currents [Goldstein and Zebker, 1987]. The spatial baseline obtained this way is small (ideally zero) and the acquired images are basically identical except for a slight difference in acquisition time, and the resulting interferogram phase is proportional to the line-of-sight displacement of each resolution element over this time interval. Such data have been compared to surface based observations, [Goldstein et al., 1989], [Marom et al., 19901, and it has been shown that velocity-sensitive interferometry can be used to obtain ocean wavenumber spectra that are in agreement with power spectra measured in situ, Currently, these techniques are evolving into the multiple baseline domain. It was recently shown that ocean coherence time can be estimated using a dual-baseline along-track interferometric system [Griffin et al., 1993; Carande, 1994].

Current developments include the use of satellite radar interferometry for studying dynamic phenomena. The first earthquake displacement estimation was reported by Massonnet et al. [19931 who combined a SAR interferogram with a Digital Elevation Model (DEM). The radar images forming the interferogram were acquired before and after an earthquake, and by removing topographic effects using an available DEM, they were able to isolate the earthquake displacement field. By combining three radar images as two pairs of interferograms Zebker et al. [1994] were able to separate topographic and dynamic effects and thus estimate the coseismic displacement field using radar data alone. They also verified the results by comparison with more conventional Global Positioning Satellite (GPS) and trilateration data. Similarly, repeat track interferometry with very small baseline, and thus little sensitivity to topography, has been used to estimate ice sheet motion [Goldstein et al., 1993].

Developments in airborne interferometry have lately addressed issues of importance for improving performance and operational utility. Processing techniques to correct for undesired platform motion, to automatically determine the multiple of 2π required to translate measured phases to the absolute phase, and to calculate target locations for squinted SAR acquisition have been developed [Madsen et al., 1992]. The theoretical performance of across-track interferometric systems, including analysis of limiting factors such as thermal noise, baseline decorrelation, temporal decorrelation etc., has been analyzed in several papers [Rodriguez and Martin, 1992], [Zebker and Villasenor, 1992], and [Rodriguez et al., 19941, and actual performance measurement verification for airborne systems have been evaluated [Madsen et al., 1994].

1.2 Introductory Discussion of SAR Interferometry Principles

SAR interferometry is fundamentally different from optical interferometry as the complex signal, both amplitude and phase, is directly available. In the optical counterpart the phase information is only available through the constructive and destructive interference patterns.

SAR interferometric principles utilized today can be separated into two basic situations: space baselines and time baselines. More complicated applications are generally a combination of multiple interferograms with simultaneous space and time baselines.

Space baselines. The generic space baseline situation is illustrated in Fig, 1. As discussed in Volume I, chapter 10, a SAR resolves targets 2-dimensionally through measurement of the pulse delay of the transmitted pulses (providing range discrimination) and by determining the Doppler history of individual targets (along-track discrimination). In this introductory section we

will consider a simplified situation where the SAR antenna fan beam [1] is oriented perpendicularly to the platform path, and the data is processed to ensure that the radar "looks" in a direction orthogonal to the platform velocity vector[2].

In the space baseline situation a target area is imaged from two different SAR tracks simultaneously (i.e. zero temporal baseline). The displacement vector from one acquisition track to the other (in the fan beam plane) is called the baseline vector. The basic measurement is the estimate of the target height from the known platform positions $\bar{r}_1 = (x, y_1, z_1)$, $\bar{r}_2 = (x, y_2, z_2)$, and the ranges measured from the SAR antennas to the target, ρ_1, ρ_2. The space baseline thus allows us to measure terrain topography. The strength of the interferometric technique compared to stereo techniques is that utilizing the phase difference of the interferogram the slant range difference, $\delta\rho = \rho_2 - \rho_1$ *can be* determined very accurately, with fractional wavelength precision. Also, since the wavelength is on the scale of centimeters and the resolution of the systems are on the order of meters, even when the change in viewing angle changes the interferometric phase significantly, the images are still precisely overlaid on a scale of the resolution cell according to a predictable pattern based on the geometry (the so-called flat Earth fringe pattern). Practical obstacles which we shall discuss below includes the conversion of an ambiguous phase measurement (which involves an unknown multiple of 2π) to unambiguous range differences. The details of the space baseline technique are discussed below in the section "Interferometric

---

1 The SAR antenna radiation pattern is usually narrow in the along-track direction and wide in the across-track direction, thus it is called a "fan-beam"

2 We note that even if the radar antenna was squinted forward or backward during data acquisition the data processing can alway reference the date (range, azimuth, and phase) to the broadside case. See appendix.

Topographic Mapping". Thus interferometric SAR is an alternative to conventional stereo photographic techniques for generating high resolution topographic maps-- the technique features automated processing, and encompasses advantages such as all-weather, night and day capability. Also, the elevation information obtained through application of radar interferometry is of other uses than topographic mapping. The simultaneous measurement of range, azimuth angle and elevation angle provides the absolute 3-dimensional location of each image point, thus radar images can be accurately transformed from the distorted slant range to cartographic ground range format. his enables the correction of radar artifacts such as foreshortening (the phenomena that targets at a higher elevation will be closer to the radar and thus they will "tilt" towards the radar in a 2-D image) and simplifies the co-registration of images acquired by different geometries and sources. It is interesting to note that the combination of one interferometric channel with simultaneously operated channels (such as multi-frequency or multi-polarization channels) will permit automatic generation of multi-channel 3-dimensional geolocated radar images.

Time baselines. The generic time baseline situation assumes that a SAR measurement acquired from exactly identical acquisition tracks is repeated at different times, $\bar{r}_1(t) = (x_1, y_1, z_1) = \bar{r}_2(t + \delta t)$. The fundamental principle is that with identical data acquisition situations the interferometric difference will be related to changes in the observed scene. One method to approximate the "perfect" time baseline is to mount two SAR antennas along the fuselage of an aircraft[3]. With a ground speed on the order of 200 m/see and along-track baselines of typically 2 to 20 meters, time baselines from 0.01 to 0.1 seconds are representative. Alternatively one can utilize measurements from satellite SAR's which repeat their orbits at

---

3 Two antennas on the same. platform (or system) spaced in the flight direction is sometimes denoted along-track interferometry (ATI).

regular intervals This technique generally results in time baselines on the order of one or more days. With a time baseline δt, a radial target velocity of u, and a wavelength λ, we measure an interferometric phase $\phi = 4\pi u \delta t/\lambda$ (4π comes from two-way propagation, assuming each channel transmits and receives using the same antenna). In the aircraft case typical baselines and system parameters will lead to a velocity sensitivity on the order of a centimeter per second (useful for ocean surface motion or vehicle traffic), while in the spaceborne case velocities of centimeters per day (appropriate for ice motion) are possible. The time baseline thus allows us to measure a velocity component in the line-of-sight direction.

Mixed baselines. If one is interested in simultaneous measurements of dynamics and topography multiple mixed baselines could be implemented on one SAR platform, This would for instance be of interest for measuring ocean dynamics, However, mixed baselines are more often encountered in satellite repeat pass applications where either spatial or temporal baselines are desired, but the complementary baseline is unavoidable,

In cases where repeat pass interferometry is used to *generate* topographic maps the temporal baseline will often cause the second image to lose coherency relative to the first image (see Zebker and Villasenor, [1992], for example), a phenomena called temporal decorrelation. This loss of coherency results from changes in the distribution in surface scatterers and will be discussed further later. The phase of repeat pass interferograms over oceans will for instance be a pure noise process if the temporal baseline is longer than a few seconds, and other surface changes in shape or dielectric constant such as freezing, thawing, vegetation movements due to wind, or surface changes due to precipitation can seriously degrade the quality of the acquired interferogram. On the

---

[4] Time baselines obtained by one platform repeating a track is called repeat pass interferometry (R'II), or multiple pass interferometry.

other hand, when studying dynamic phenomena the spatial baseline is a nuisance since it will add a phase contribution which depends on the scene topography.

In cases where both spatial and temporal baselines are significant multiple pairs of baselines can sometimes be used to separate topographic and dynamic components. If an approximately instantaneous dynamic phenomenon (e.g. an earthquake) is being studied, two images both acquired either before or after the change can be used to estimate the topography, enabling the topographic phase term to be subtracted when forming an interferogram of two images acquired before and after the change. In other situations where continuous movements are being monitored different interferometric pairs will usually have different ratios between the spatial and the temporal baselines and thus different sensitivities to topography and dynamic phenomena, This will be discussed in more detail in the section “Change Mapping”.

2 Interferometric Topographic Mapping

2.1 Single pass interferometry

The phase of the who received in channel i from a target, T, is given by,

$$\phi_i = -\frac{2\pi}{\lambda}(\rho_{ti} + \rho_{ri}) = \phi_{ti} + \phi_{ri} \tag{1}$$

where t,r indicates transmission and reception respectively. If an interferogram is formed from two images which share a common transmitter then only one-way propagation differences (the differences in the receive path) are reflected in the interferogram; if on the other hand each channel uses one antenna for transmitting and receiving then two-way propagation applies. When an interferogram is formed by co-registration of two complex images and multiplication of each pixel of channel 2 with the complex conjugate of channel 1 we have for the interferometric phase,

$$\phi = \phi_2 - \phi_1 = -\frac{2\pi}{\lambda} p(\rho_2 - \rho_1) \tag{2}$$

where $p = 1$ when the channels share the transmit antenna, $p = 2$ if each channel is transmitting and receiving on one channel specific antenna. The phase measured in the interferogram, ϕ_M, is the modulus of the absolute phase of equation (2),

$$\phi_M = \mathrm{mod}(\phi, 2\pi) \tag{3}$$

The problem of getting from ϕ_M to #1, so-called phase-unwrapping and absolute phase determination, will be discussed later, Assuming the geometry of Fig. 1, we have

$$\rho_2^2 = \rho_1^2 + B^2 - 2\rho_1 B\cos(\theta - 0_{21}) \tag{4}$$

where B is the length of the displacement. Introducing the horizontal baseline angle $a = \theta_{21} - \pi/2$, the look angle and the interferometric phase are related by

$$\sin(\theta - a) = \cos(\theta - \theta_{21}) = \frac{\rho_1^2 - \rho_2^2 + B^2}{2\rho_1 B}$$
$$= \frac{(\rho_1 - \rho_2)(\rho_1 + \rho_2)}{2\rho_1 B} + \frac{B}{2\rho_1} \qquad (5)$$
$$\cong \frac{(\rho_1 - \rho_2)}{B} = \frac{\lambda\phi}{2\pi p B}$$

In the last line we made an approximation which is valid when the baseline is small compared to the slant range. We will use that approximation in the following as it is usually a good approximation, it makes expressions more intuitively understandable, and the more accurate expressions are in any case easily introduced when required. It is now trivial to solve for the target height and across-track position:

$$\theta = a + \arcsin\left(\frac{\lambda\phi}{2\pi p B}\right) \qquad (6)$$

$$h = H - \rho_1 \cos\theta \qquad (7)$$

$$y = \rho_1 \sin\theta \qquad (8)$$

From (6) it is obvious why same antenna transmission and reception, $p = 2$, is sometimes called baseline doubling. Note that the accuracy of the small baseline approximation can be improved if one introduces a reference point which is halfway between the two antennas, and uses $P^2 + (A^2 + \rho_2^2 - B^2/2)/2$ as the slant range in (7) and (8).

A more general geometry allowing for non zero Doppler geometry is discussed in Madsen et al. [1993]. Using a track reference halfway between the two antennas and writing $\hat{n}_{los}$ for the line-of-sight unit vector pointing from the track reference to the target, the three basis equations are:

$$\bar{r}_{target} = \bar{r}_{radar} + \rho\,\hat{n}_{los} \qquad (9)$$

$$f_D = \frac{2}{\lambda}\hat{n}_{los} \cdot \bar{v} \qquad (10)$$

$$\phi = \frac{2\pi p}{\lambda} \hat{n}_{los} \cdot \vec{r}_{21} \tag{11}$$

where (9) gives the target location in terms of the reference position, the slant range, and the line-of-sight direction, (1 O) gives the relation between the Doppler shift, f_D, the line-of-sight direction and the velocity vector $\vec{v}$, and (11) gives the relation between the interferometric phase, the line-of-sight direction and the baseline vector.

A topographic data set of the Ft. Irwin area in southern California, collected with the JPL/NASA TOPSAR system and processed based on principles as indicated above is shown in Fig, 2. This sample digital elevation model shows an approximately 35 by 35 km area in the southern California desert near Ft. Irwin, north of the city of Barstow. This data set consists of a mosaic of five strips from the instrument, three acquired with a heading of 270° and two with a heading of 90°. Contours every 40 m are shown, with darker contours every 200 m. The data are processed to 5 m post spacing.

Performance limitations. To derive accurate topographic data both vertical and horizontal accuracies are important, That the two are closely coupled can be seen if we consider terrain with slope, β, then any horizontal position error will translate into a height error of $\sigma_{vert} = \tan\beta \, \sigma_{hor}$. Since the radar topography map is intrinsically co-registered with the radar intensity image, any recognizable features such as road intersections, buildings, and the like will also be misplaced horizontally, An in-depth analysis of error sources is outside the scope of this text the reader is referred to [Rodriguez and Martin, 1992], [Zebker and Villasenor, 1992], [Zebker et al., 1994a] and [Rodriguez et al., 1994]. However, some important performance limiting factors are obvious 6om equations (6), (7), and (8).

Phase noise is introduced by finite signal-to-noise-ratio (SNR) and impulse response sidelobes. Assuming the two image channels have the same SNR, but independent noise, the phase noise level is approximately,

$$\sigma_\phi = \sqrt{\frac{1}{SNR}} \tag{12}$$

which translates into an angular error of

$$\sigma_{\theta|\phi} = \frac{\lambda}{2\pi pB}\frac{\sigma_\phi}{\cos(\theta - a)} = \frac{\lambda}{2\pi pB_\perp}\sigma_\phi \tag{13}$$

where we introduced the baseline orthogonal to the look direction, $B_\perp = B\cos(\theta - \alpha)$. An additional angular error is introduced if navigation data used for determining the baseline attitude (which will vary dynamically thus requiring motion compensation) indicates the wrong angle *a, as this* translates into an incidence angle error

$$\sigma_{\theta|\alpha} = \sigma_\alpha \tag{14}$$

In either case an error in θ will result in height and cross-track errors, as

$$\sigma_{h|\theta} = \text{psin O}\,\sigma_\theta \tag{1s}$$

$$\sigma_{y|\theta} = \rho\cos\theta\,\sigma_\theta \tag{16}$$

The effects of phase and attitude errors are, however, quite different. The phase errors vary from point to point within the image and are referred to as high-frequency statistical errors. The errors in baseline attitude, though, lead to tilts in the overall height maps and are referred to as systematic errors, Baseline errors are highly correlated from point to point and can be corrected using known tie points within an imaged scene.

As an example, a 20 dB SNR, 5 cm wavelength, common transmitter antenna and a 2.5 m baseline will produce an angular error of 0.32 mrad = 0.018°, which corresponds to a 4 m horizontal and vertical error at 45° incidence angle and a platform height of 12.5 km.

A much used technique to improve the noise performance of an interferometer is to utilize multiple "looks", usually implemented by spatial averaging of the complex interferogram. Multi-looking reduces the phase noise by $\sqrt{N_L}$, where N_L is the number of independent samples averaged, at the expense of a reduced spatial resolution. The averaging will, however, not improve on the systematic errors such as those introduces by motion compensation errors.

A less intuitive error source is that of baseline decorrelation. Baseline decorrelation originates from the fact that not all targets within the resolution cell contribute the same interferometric phase. If in fact the baseline is so large and the range resolution is so poor that the contributions from a single resolution cell can take any value between minus and plus π then the resulting interferogram phase will be completely random. It is said that the critical baseline has been reached. Useful interferometric data can only be obtained if the actual baseline is significantly less than the critical baseline. If we assume that all targets are at a reference height (thus $\rho = H/\cos\theta$) one easily finds the interferometric fringe rate from equation (5),

$$\frac{\partial\phi}{\partial\rho} = \frac{\partial\phi}{\partial\theta}\frac{\partial\theta}{\partial\rho} = \frac{2\pi\, p\, B}{\lambda}\cos(\theta-\alpha)\frac{1}{\rho\tan\theta} \tag{17}$$

Defining the critical baseline as the baseline corresponding to a fringe rate of 2π per range resolution cell, we have

$$\begin{aligned} &\frac{\partial\phi}{\partial\rho}\Delta\rho = 2\pi \Rightarrow \\ &B_{c\perp} = B_c\cos(\theta-\alpha) = \frac{\rho\lambda\tan\theta}{p\Delta\rho} = \frac{\rho\lambda}{p\Delta y\cos\theta} \end{aligned} \tag{18}$$

where we introduced the slant range resolution, $\Delta\rho$, and the ground resolution, Ay = $\Delta\rho/\sin$ 8. A more thorough analysis will show that this baseline decorrelation is related to the property that the different look angles of the interferometric channels result in different ground projected wavelengths even though the radar wavelengths are identical. Thus the baseline decorrelation can be reduced if the two interferometric channels are offset in frequency such that the ground projected wavelength is kept constant, This was first pointed out by Gatelli et al. [1994].

In relation to aircraft interferometry the issue of motion compensation is particularly important, A thorough discussion of the errors resulting from incorrect navigation data or from deficiencies in the motion compensation algorithms applied is beyond the scope of this text, and we will only mention the major issues here. Ideally the radar platform would move along a smooth reference track such as a straight line or a great circle arc. Errors in the platform position will translate into target position errors as seen from equation (9). Velocity errors on the other hand lead to rotations and tilts of the topographic data. Dynamic errors (e.g. sinusoidal position or attitude errors) will result in unfocused images with poor geometric fidelity, and wrong baseline attitudes will reflect itself as vertical and horizontal errors in the output data. A difficulty in implementing perfect motion compensation is that to correct signal delay and phase for deviations between the actual and the reference track one needs the line-of-sight-vector to the target which is, however, not known until the topographic data has been processed. Motion compensation is discussed in more detail by Ma&Met al. [1993] and the accuracy of airborne interferometric SAR's with navigation errors present is discussed by Rodriguez et al. [1994].

Phase unwrapping and absolute phase determination. In the above we have assumed that we have available the absolute phase, ϕ, even if we only measure ϕ_M, as indicated in equation (3). The process of converting ϕ_M to ϕ consist of two steps, phase unwrapping and absolute phase determination. Phase unwrapping is discussed by Goldstein et al. [1988], but we

will illustrate the principle here. Let us in this section normalize ϕ by dividing by 2π such that its units are cycles and ϕ_M varies from O to 1 (one not included). An intuitive method for phase unwrapping is to ensure that the phase jump from one pixel to its neighbor is less than 0.5 cycles, that is, the data are all adequately sampled. The one dimensional measurements 0.0,0.1,0 .9,0.8 would "unwrap" to 0.0, 0.1, -0.1, -0.2, 'he situation is unfortunately less straight forward when real 2-D problems (with noise and discontinuities in the true phase due to layover[5]) are analyzed. Consider the measurement matrix

0.2	0.2	0.2	0.2
0.4	0.2	0.2	0.4
0.6	0.8	0.8	0.6
0.8	0,8	0.8	0.8

We will first unwrap this data set using an algorithm which first unwraps column one and then unwraps each row using column one as the starting point for a 1-D unwrapping. In this case the result of the unwrapping is the same as the input. Next, we unwrap the data using an algorithm which first unwraps row one, then unwraps each column using row one as the starting point for a 1-D unwrapping, The result is

0.2	0.2	0.2	0.2
0.4	0.2	0.2	0.4
0.6	-0.2	-0.2	0,6
0.8	-0.2	-4.2	0.8

which is different from the previous result. The problem can be traced to so-called residue points. A residue point is a point where the sum of the phase differences of a circular unwrapping of four

---

5 Layover is related to foreshortening mentioned earlier, Layover is the situation when a target, which in ground range is further away from the radar than another target, will appear closer to the radar in the slant range image due to a higher elevation.

points in a 2 by 2 rectangle is not zero, but PIUS or minus one cycle of phase, There are two such residues in the above example, The 2 by 2 subwindow

0.4 0.2
0.6 0.8

encloses a negative residue, and the 2 by 2 subwindow

0.2 0.4
0,8 0.6

encloses a positive residue. Now, if we connect negative and positive residues with "cut lines" which cannot be unwrapped across, any permissible closed unwrapping path will enclose a sum of residues which is zero and the unwrapping will be consistent independent of the starting point and unwrapping direction. We woutd like to stress that mapping out the residue points of an interferogram is a unique process. However, defining the "cut-lines" is not a unique process and algorithms to connect residues in an optimal way are still being studied.

After determining the residues, defining the cut-lines, and performing the actual phase unwrapping we have an approximation for the absolute interferometric phase which only differs from the absolute phase by a integer number of cycles. Note that this integer is a single number for the entire region unwrapped. A simple manual method to determine this constant is to find one target in the interferogram where the target position, including the height, is known. Using this information the remaining integer number of phase cycles can be found, It is however of much utility to obtain this value from the data directly without foreknowledge of the surface. Different automatic algorithms have been used to determine the residual cycle offset. One algorithm relies on forming higher order unambiguous interferograms from the measurements. If for instance the received range bandwidth is divided into two subbands which are processed separately, and a new interferogram is formed from the high and the low carrier frequency interferograms, then an

interferogram which has a carrier frequency equivalent to the difference of the subbands is obtained. This low frequency interferogram is generally unambiguous, but noisy, and it can be used to solve for the unknown number of integer cycles if enough points can be averaged to reduce the statistical noise. Alternatively, one can note that the absolute interferometric phase is a measure of the range offset of one channel of the interferometric pair with respect to the other. Thus using the unwrapped interferogram as a measure of the absolute phase one can resample one channel with respect to the other very accurately. Any number of phase cycles not included in the unwrapped phase will lead to an off-set of one image with respect to the other which is constant over the entire area unwrapped but typically very small. Using precision correlation techniques which estimate image co-registration errors on the order of a few thousands of a pixel allows the automatic determination of the remaining number of phase cycles.

Corrections for spherical geometry. Even though the basic principles do *not* change when considering spherical geometry some modifications must be applied to the formulation of interferometric data analysis, These corrections are not only necessary for satellite applications but also for precision aircraft measurements. We have found it very useful to operate with a spherical Earth system which we call an (s, c, h) system, were s is an along track-coordinate, c is an across-track coordinate, and h is the height above a sphere with radius, R_o. The s and c coordinates are measured at the surface of the sphere, A convenient property of the (s, c, h) system is that most problems can be formulated in term of rectangular coordinates (x, y, z) and then converted to an appropriately defined (s, c, h) system. A mathematical definition of the (s, c, h) system is provided in the appendix. In rectangular coordinates equation (9) is,

$$\begin{aligned} x_{target} &= x_{radar} + \rho(\hat{n}_{los})x \\ y_{target} &= y_{radar} + \rho(\hat{n}_{los})_y \\ z_{target} &= z_{radar} + \rho(\hat{n}_{los})_z \end{aligned} \tag{19}$$

where $(\hat{n}_{los})$X is the x-component of the line-of-sight unit vector, etc. The corresponding equations in the (s, c, h) system are

$$
\begin{aligned}
h_{target} &= h_{radar} + \rho(\hat{n}_{los})_h + \frac{\rho^2\left((\hat{n}_{los})_s^2 + (\hat{n}_{los})_c^2\right)}{2\left(R_a + h_{radar} + \rho(\hat{n}_{los})_h\right)} \\
s_{target} &= s_{radar} + \rho(\hat{n}_{los})_s \frac{R_a}{\left(R_a + h_{target}\right)} \\
c_{target} &= c_{radar} + \rho(\hat{n}_{los})_c \frac{R_a}{\left(R_a + h_{target}\right)}
\end{aligned}
\tag{20}
$$

In the following we will discuss formulations in (x, y, z) coordinates to keep the equations simple,

2.2 Two-pass interferometry

Often data acquisition limitations necessitate that the images of an interferometric pair is acquired at different times. This is for example the case today with satellite systems, as a dedicated single pass interferometric SAR satellite ha.. not been flown as yet. If, however, the target area has not changed between passes there are no fundamental problems with generating across-track interferograms from data sets acquired at different times. Also, the repeat-track approach allows much flexibility which is not practical with multiple antennas on one platform. For instance, it is possible to synthesize large baselines with multiple passes which would not be feasible on a single platform, In a later section we will return to the possibilities offered by combining several baselines.

There are further complications to be considered when separate radar passes are used to form interferograms. Some of the most important issues are:

- The baseline (length and orientation) is usually not known with the required accuracy

- The tracks are usually not exactly parallel, in other words the baseline changes with the along-track position
- The target area might have changed between data takes, so-called temporal decorrelation
- Aircraft case: motion compensation is much more difficult and critical than in the single pass case

Estimation of the baseline. The most ideal situation is of course that the accuracy of the navigation data is sufficient to allow direct determination of the baseline with the required accuracy. The "required accuracy" is an ambiguous term. Them is one accuracy requirement to allow the image pair to be registered accurately enough to form a high quality interferogram. In this case the baseline knowledge across-track should be a small fraction (typically better than a tenth) of the slant range resolution, and the along-track baseline should correspondingly be known to an accuracy of a fraction of the azimuth resolution. The baseline accuracy to allow the absolute phase interferogram to provide absolute heights with the required accuracy is, however, much more difficult to meet, as the relative baseline accuracy, 0_{θ}/B, has to be on the order of the position accuracy required relative to the slant range, $|\sigma_r|/\rho$, which is typically in the range 10^{-4} to 10^{-6}. This is usually not attainable even with differential GPS techniques and tie-points in the image are therefore required to perform the final alignment of the topographic data. We will here *outline the* baseline estimation proms by considering the most common ease, where the navigational data is not even sufficiently accurate for the image co-registration, however, the terrain is already covered by a low resolution topographic map. In a coordinate system aligned with the track of pass-one, pass-one is given as

$$\bar{r}_1(s_1) = \begin{pmatrix} 0 \\ 0 \\ H \end{pmatrix} + s_1 \Delta x \begin{pmatrix} 1 \\ 0 \\ 0 \end{pmatrix} \qquad (21)$$

where s_1 is the pulse number, H is the nominal height, and Δx the along-track pulse spacing. The corresponding expression for pass-two is,

$$\bar{r}_2(s_2) = \begin{pmatrix} x_{02} \\ y_{02} \\ H + z_{02} \end{pmatrix} + s_2 \Delta x \begin{pmatrix} (1 + \gamma_2) \\ \partial y / \partial x \\ \partial z / \partial x \end{pmatrix} \qquad (22)$$

where (x_{02}, y_{02}, z_{02}) are the baseline off-sets at $s_2 = 0$, γ_2 is the scale difference, and $\partial y / \partial x$ and $\partial z / \partial x$ are the track divergence in y and z. Note that γ_2, $\partial y / \partial x$, and $\partial z / \partial x$ will be very small for any useful data set. The estimation is based on measured off-sets in along-track,s, and across-track, ρ, coordinates for a number of targets recognizable in both images. This is typically done automatically using registration techniques on the intensity images or using a fringe visibility criteria (see, for example, Zebker et al. [1994a]), The result is a list of along-track and range coordinates, $(s_1, \rho_1, s_2, \rho_2)$, *with N* entries, one for each point or subwindow analyzed. If we know the height of each target, *i*, approximately (this is really not very critical), we can determine the i'th slant range plane which is defined by the track line of pass-one and the i'th target[6], and we can project (21) and (22) onto this (x, k) system where k is the slant plane across-track coordinate. The slant range plane geometry is shown on Fig. 3.

---

6 The incidence angle of the slant range plane of the i'th target is $\cos\theta_i = (H - h_i)/\rho_{1i}$

By projecting the coordinates of the i'th target expressed by both track one and track two coordinates onto the i'th slant range plane, we find[7]

$$\begin{pmatrix} s_{i1}\Delta x \\ \rho_{i1} \end{pmatrix} = \begin{pmatrix} x_{02} \\ \sin\theta_i\, y_{02} - \cos\theta_i\, z_{02} \end{pmatrix} + s_{i2}\Delta x \begin{bmatrix} (1+\gamma_2) \\ \sin\theta_i\, \partial y/\partial x - \cos\theta_i\, \partial z/\partial x \\ -\sin\theta_i\, \partial y/\partial x + \cos\theta_i\, \partial z/\partial x \end{bmatrix} + \rho_{i2} \begin{pmatrix} 0 \\ 1 \end{pmatrix} \tag{23}$$

In terms of the parameter vector, P (the 6 unknowns),

$$\mathrm{P} = \left(x_{02}, y_{02}, z_{02}, \gamma_2, \frac{\partial y}{\partial x}, \frac{\partial z}{\partial x} \right)^T$$

the sensitivity matrix, T, with 2N rows (N being the number of targets)

$$\mathbf{T} = \begin{pmatrix} \vdots & & & & & \\ 1 & 0 & 0 & s_{i2}\Delta x & -\rho_{i2}\sin\theta_i & \rho_{i2}\cos\theta_i \\ 0 & \sin\theta_i & -\cos\theta_i & 0 & s_{i2}\Delta x \sin\theta_i & -s_{i2}\Delta x\cos\theta_i \\ \vdots & & & & & \end{pmatrix}$$

and the observation vector, O, also with 2N equations

$$\mathbf{O} \cong \begin{pmatrix} \vdots \\ (s_{i1} - s_{i2})\Delta x \\ \rho_{i1} - \rho_{i2} \\ \vdots \end{pmatrix}$$

then the least squares solution for the baseline parameters, is

$$\mathbf{P} = \left(\mathbf{T}^{\mathbf{T}}\mathbf{T}\right)^{-1}\mathbf{T}^{\mathbf{T}}\mathbf{O} \tag{24}$$

---

[7] In a zero Doppler geometry, we have from equation (22) and Fig. 3 that the line-of-sight vector for pass 2 in the slant range plane is, $n_{los,2} \cong \left(-\sin\theta_i\, \partial y/\partial x + \cos\theta_i\, \partial z/\partial x, 1\right)^T$ (the T superscript indicates transpose).

Note that if 0, is basically the same for all targets (this is the case if a narrow swath satellite data set is processed) then the outlined estimation scheme can be ill behaved, In that case it can be necessary to constrain the baseline solution. However, in this situation the precise estimation of all baseline components is also less critical in relation to co-registration before interferogram formation,

Non-parallel tracks. In cases where the tracks are nearly parallel, the estimated model parameters provides the information required to interpolate the pass-two data set to the pass-one data set so that they will register appropriately. With minor modifications one can also interpolate both data sets to a reference line which is half way between the two actual tracks, Note that since the two passes are not parallel, both the range and the azimuth shifts required will be a function of across-track as well as along-track location. During the interpolation one can remove a phase shift such that all targets at a chosen reference height will have a constant interferometric phase. This means that phase variations in the interferogram are related to topographic effects (or, noise) and this interferogram flattening can greatly improve phase unwrapping, and it is atso important if the interferogram is low-pass filtered before the phase unwrapping, After phase unwrapping and filtering the removed phase must be put back into the interferogram, before it is used to determine locations (e.g. from equations (7) and (8)).

The remainder of the processing required for two-pass topographic mapping is in principle identical to the single pass situation. However, a large track divergence makes the situation somewhat different as the actual baseline and thus the topographic accuracy can vary significantly along-track, which must be taken into account during processing, as well during data utilization.

An example of a topographic data set generated from complex SAR images acquired by the European ERS-1 satellite is shown on Fig. 4. This perspective view was generated from data

acquired over a region in the Mojave Desert in California which includes the Pisgah lava flow, visible near the scene center.

Additional complexities arise when the tracks cross at truly large angles. In extreme cases the tracks can actually cross-over and there will be an along-track position where the effective baseline is zero. Since this geometry is not useful for large scale mapping and remains the province of specialized studies, the interested reader is referred to Gabriel and Goldstein [1988] for details.

Performance limitations. Two-pass interferometry suffers from decorrelation mechanisms in addition to SNR, baseline decor-relation, navigational errors, and motion compensation errors, as already mentioned in section 2.1. Additional considerations includes first of all temporal decorrelation, and more severe navigation and motion compensation problems.

Temporal decorrelation occur when the distribution of scattering centers and thereby the interference phase of an individual resolution cell changes. Examples of change mechanisms and typical decorrelation times are:

- Geologic changes -many years
- Weathering, rain, freeze/thaw cycles -hours to years
- Man made changes -hours to years
- Vegetated areas -days/weeks
- Trees moving in the wind -seconds
- Water motion of ocean and lake surfaces -seconds

Correlation for various types of surfaces has been analyzed by Zebker and Villasenor [1992] and Zebker et al., [1994a]. Analysis showed that for 24 cm wavelength observations, such as the SEASAT SAR system, correlation would remain constant over a 20 day observation period for a desert area such as Death Valley, relatively unaffected by precipitation or vegetation growth, whereas the study of an Oregon forest showed correlation decreasing approximately linearly with

time to 0.45 after 20 days. Results from this study are shown in Fig. 5, where correlation is plotted versus time. The figure also shows a similar, though less marked, reduction in correlation for lava flows located near the Oregon forest terrain.

Analysis of ERS-1 data with a 5.7 cm wavelength yields a more widely varying set of results which in all likelihood would have been observed in the SEASAT data had more data been available to analyze. Analysis by Zebker et al. [1994a] of areas in Alaska with more severe weathering indicated that correlations are often unacceptably low, and that temporal decorrelation will often prevent the generation of useful topographic data set. This is illustrated in Fig, 6, where the average correlation in 6a (with a six day baseline) is considerable higher than 6b (with a three &y baseline), The difference is explained if we examine a plot of temperature versus time over the time intervals in question, Both of the six day baseline measurements were acquired at above freezing surface temperatures, while the three day baseline includes one above and one below the freezing point. Since freezing markedly changes the dielectric properties of the surface, the interferometric phase between passes is uncorrelated. This sort of environmental modulation precludes any simple linear estimate of the correlation of the signals with time. On the other hand, analyses of ERS-1 data in desert areas of the southwest US has shown correlations greater than 0.5 over periods of up to one full year.

In the case of aircraft two-pass interferometry it is found that requirements on the navigation data and the motion compensation algorithms applied are extremely demanding. In the single pass situation most navigation errors and motion compensation algorithm approximations will give rise to common mode errors. These common mode errors thus have minor impact on the quality of the interferogram. This situation is completely different in the two-pass situation where the navigational errors on each pass will be independent and motion compensation algorithms likewise,

2.3 Systems for topographic mapping

There arc today data available from a number of systems which can be used for topographic interferometric radar mapping. The list is growing rapidly as this is being written and it is very likely that there are systems planned which we are not aware of, The single pass aircraft systems of JPL and the Canada Centre for Remote Sensing have generated extensive data sets for a number of years, they will be described briefly below. The Environmental Research Institute of Michigan has since 1993 developed a dedicated high performance topographic mapping system, which is now being tested, [ERIM, 1994]. Also, Norden Systems, United Technologies, has developed a testbed system, [Fullman et al., 1994]. In Europe the Technical University of Denmark and Dornier, Germany, are known to be developing similar systems.

Satellite systems which have generated significant amounts of repeat pass interferometric data are the U.S. SEA SAT (1978) L-band system, the European ERS-1 (199 l-now) C-band system, and the Japanese J-ERS-1 (1992-now) L-band system.

2.3.1 Aircraft single pass systems

The TOPSAR system uses the C-band channels of the JPL/NASA AIRSAR DC-8 airborne synthetic aperture radar system, and the CCRS system uses the C-band channels of the CCRS Convair CV-580 airborne synthetic aperture radar system. Both systems have been used to develop topographic mapping techniques and for application studies in areas such as geology, glaciology, hydrology, and forestry. Basic system parameters are shown in Table. 1.

TOPSAR for instance utilizes two antennas which are flush mounted on the left side of the DC-8. The antennas are mounted at the same along-track position with a separation (baseline) in the across-track plane of 2.5 m. The foresights of the antennas are depressed 45° with respect to horizontal, One antenna is used for transmission and the signals received by both antennas are

recorded independently. The slant range resolution of the system is limited by the system bandwidth (40 MHz) to 3.75 m and the slant range swath width after range compression is 9.5 km. Data can also be acquired at a 7.5 m resolution, in which case the swath after range compression is more than doubled.

The NASA DC-8 is equipped with a number of navigation systems. Position, attitude determination, and motion compensation is extremely important thus the radar instrumentation includes two inertial navigation systems, one, a Honeywell H-764G, has an embedded P-code GPS[8] system. This system provides both accurate position (better than 15 m), very accurate attitude parameters and a high update rate for motion compensation purposes. The navigation suite also includes two differential GPS systems, one of them a kinematic Turbo Rouge system which provides off-line estimates of the aircraft position with decimeter accuracy.

The TOPSAR system has been semi-operational since 1991 and has collected extensive data sets in the U.S., in Europe, and in South America, Fig, 7 is a mosaicked digital elevation model for the Galapagos Islands acquired by the TOPSAR system, The CCRS topographic mapping system has been operating since 1992. Fig. 8 shows a perspective view of a topographic data set acquired by the CCRS over a glacier on Bylot Island, North West Territories, Canada.

2.3.2 Two-pass satellite systems

The systems mentioned here can only generate interferometric data through the combination of complex images acquired on separate passes. System parameters for these satellite systems are shown in Table 2.

---

8 P-code GPS, refers to the satellite based, dual frequency precision code channel of the U.S. Global Positioning System.

The SEASAT satellite, launched in 1978, collected large data sets during its 100 day life time which became the key source of satellite SAR data until the launch of the European ERS-1 satellite in 1991.

The ERS-1 satellite was launched by the European Space Agency (ESA) in July 1991, ERS-1 is still operational today, 3 years later. ERS-1 is planned to be succeeded by a nearly identical satellite, ERS-2 to be launched early 1995. ERS-1 data has been used by numerous organizations for interferometric SAR studies. The ERS-1 satellite is particularly well suited for interferometry because of it well maintained orbit, which makes it very likely that repeated orbits are sufficiently close to be useful for interferometry.

The J-ERS-1 satellite was launched by the Japanese Space Organization, NASDA, in 1992. The J-ERS-1 orbit is not as well maintained as ERS-1, thus the system has generated less interferometric data sets despite the fact that the critical baseline is somewhat larger at L-band than at C-band.

2.4 Applications for topographic radar data

Among the studies requiring continental topographic data are hydrology, ecology, glaciology, geomorphology, and atmospheric circulation, [Evans et al., 1992], [Farr et al., 1994]. For example, in hydrologic and terrestrial ecosystem studies, topography exerts significant control on intercepted solar radiation, water runoff and subsurface water inventory, microclimate, vegetation type and distribution, soil development, and a host of additional interdependent parameters, The topography of the polar ice caps and mountain glaciers is important because it directly reflects ice-flow dynamics and is closely linked to global climate and sea-level change. Monitoring the amplitude of seasonal advance and retreat of mountain glaciers on a global basis and longer term trends of the polar ice sheets can give important information on the rate of global warming.

Accurate mapping of the forms and slopes of young geomorphic features such as glacial moraines and feature offsets and scarps due to recent geological faulting can provide new information not only on the formative tectonic processes but also on the climatic and paleoclimatic processes contributing to their present form. Furthermore, models of the present and past general circulation of the atmosphere require topography as a fundamental input.

NASA has sponsored two working groups, entitled the Topographic Science Working Group [TSWG, 1988] and the Joint Topographic Science Working Group, to review previous panel reports and recommend a strategy for generating high resolution, accurate digital elevation measurements of the entire land and ice surface of the Earth in a single consistent reference frame. The Joint Topographic Working Group, in particular, addressed horizontal and vertical resolution requirements for various disciplines. The working group report is still unpublished in its entirety, but a summary of their findings is presented in Fig. 9. This figure emphasizes the wide range (over several orders of magnitude) of requirements. Nevertheless, some common features stand out. First, several disciplines require very high resolution topographic data with horizontal resolution of a few tens of meters (approximately the resolution of current high resolution space-based imaging systems such as Landsat TM and SPOT) and vertical precision of several meters or better. High vertical precision (a few decimeter) over the polar ice sheets is particularly important to enable mass balance studies, Here, high horizontal resolution is less critical because slopes are generally lower, so widely separated measurements or averages over a few hundred meters do not, in general, cause large height biases.

Examination of Fig. 9 shows that many of the investigations would be enabled if elevation data at a vertical accuracy of 2-5 m and a spatial resolution of 30 m were available, requirements satisfied by existing technological limitations of radar interferometry. The principal exceptions

here are the polar ice studies, which do not require fine spatial resolution but do need very precise vertical accuracies for adequate calculation of ice volumes.

Existing systems generate data commensurate in accuracy with the best commonly available data. For example, the JPL/NASA TOPSAR system exhibits errors of about 1 m rms in flatter regions and 3 m rms in mountainous areas of moderate relief. The sample digital elevation model depicted in Fig. 2 above has been analyzed and shown to be accurate to these levels.

The error distribution and levels achieved in interferometric data sets are illustrated in Fig. 10, which shows the difference between data collected by TOPSAR on a separate collection near Ft. Irwin and a 7 by 7 km square reference DEM generated by the Army's Topographic Engineering Center (TEC). The reference had an accuracy of better than 0.3 m vertical resolution at 5 m post spacings. The quality evaluation provided the aforementioned accuracy of 1 m rms in the flat areas, degrading to 3 m rms in the mountains. The standard United States Geological Survey (USGS) product generally available for this area at a 30 m post spacing is characterized by a desired accuracy level of 7 m.

The ability of interferometric radar instruments to acquire data over remote areas is demonstrated in Fig. 7 and 8. Fig. 7a, shows a mosaic of the Galapagos islands of Femandina and Isabela. This mosaic was assembled from about 20 aircraft passes and maps an area over 100 km long. This is the best existing elevation model of the region, which is difficult to get to and does not support complicated logistics easily. The interferometer required minima! considerations to weather and the data for the mosaic were collected in a single day's flying with the aircraft based on the mainland 1000 km away, An error map estimate derived from the observed correlation values is shown in Fig. 7b. Fig. 8 shows an image of a remote glacier on Bylot Island, NWT, Canada, as mapped by the CCRS aircraft system. It is interesting to note that the resolution, horizontal as well as vertical, is sufficient to outline individual morainnes.

3 Velocity Mapping

3.1 Theory and Algorithms of Along-track interferometry

Consider two antennas spaced a distance B along the fuselage of an aircraft. We assume the fan beams are oriented orthogonally to the platform velocity vector. At a velocity v the rear antenna will occupy the position of the front antenna, with a time lag of B/v, Typical baselines of 2 to 20 m and a ground speed on the order of 200 m/see corresponds to time lags on the order of 0,01 to 0.1 sec. One can use each antenna to both transmit and receive, or one antenna can be used for transmission and reception while a second antenna is used for reception only, the latter situation equivalent to transmitting and receiving from an antenna halfway between the actual transmit and receive antennas. By shifting one image appropriately with respect to the other and forming an interferogram, one finds for the interferometric phase,

$$\phi = -\frac{2\pi p u \delta t}{\lambda} = -\frac{2\pi p u B}{v\lambda} \qquad (25)$$

where $\delta t = B/v$ *is the* time delay, u the radial target velocity, p is 1 or 2 depending on the transmitter/receiver setup, and λ is the wavelength. A simple calculation will show that a 10 m baseline, 0.25 m wavelength, 200 m/sec platform velocity, and a 20 dB SNR corresponds to a single-look velocit y resolution on the order of 8 cm/see, which is typically improved by an order of magnitude through multi-looking (multi-looking is for instance achieved by spatially averaging measurements).

At an incidence angle θ the line-of-sight velocity is

$$u = u_y \sin\theta - u_z \cos\theta \qquad (26)$$

where (u_y, u_z) *are. the* across-track and vertical velocities Usually it is assumed that the average value of the vertical velocity is *zero in* which case we have,

$$u_y \cong \frac{u}{\sin\theta} \tag{27}$$

In a system where the transmission is toggled between the front (F) and the aft (A) antenna while receiving on both simultaneously, four channels are obtained, FF, FA, AF, AA (where FA for instance indicates A transmission and F reception). Generating an interferogram from the FF and AA channels will provide a baseline which is twice as long as by combining FF with FA or AF, or by combining AA with AF or FA. In addition to measuring the average velocity of each resolution cell multiple time baselines allow the estimation of the ocean decorrelation time. We define the correlation of complex signals c 1 and c2 from channels 1 and 2 as,

$$\gamma(t) = \frac{\langle c_1 c_2^* \rangle}{\sqrt{\langle c_1 c_1^* \rangle \langle c_2 c_2^* \rangle}} \cong \frac{\sum c_1 c_2^*}{\sqrt{\sum c_1 c_1^* \sum c_2 c_2^*}} \tag{28}$$

where the summation is evaluated over a small window such that the mean value of the interferogram does not change significantly.

We assume the correlation as a function of time can be modeled by,

$$\gamma(t) = \gamma_0 \exp\left(-\frac{t}{\tau_c}\right) \tag{29}$$

---

9 The technique discussed here will not allow the measurement of the along-track velocity component. A system with a squinted beam will, however, measure the velocity in the look direction and it is conceivable to design a system with beams squinted both forward and backward such that both the across- and the along-track components can be estimated.

where the decorrelation at zero time lag is due primarily to SNR. Evaluating the correlation at two time lags we have,

$$\tau_c = \frac{2}{\ln\left(\gamma(t_1)/\gamma(t_2)\right)} \quad (30)$$

The correlation measurement is important to characterize many surface processes such as eddies, upwelling or other chaotic phenomena.

3.2 Systems for velocity mapping

To our knowledge only JPL and Norden Systems has demonstrated and published results from experiments with along-track interferometric modes. However, the Canadian Center for Remote Sensing is known to be updating that system with a similar capability,

The JPL along-track interferometric system utilizes the L- and C-band channels of the JPL/NASA AIRSAR system. Top-level system parameters are presented in Table 3. The available navigation systems are the same as those discussed in section 2.3.1. The Norden Systems radar is a Ku-band system, mounted in the nose radome of a Gulfstream G-11 aircraft. The antenna beam is squinted forward when mapping in the along-track mode and has multiple receive apertures which allow for dual simultaneous time lags, [Griffin et al., 1993].

Satellite systems with velocity measurement capabilities, have not been presented at this point in time,

3.3 Applications for velocity mapping radar

Currents mapping applications have received the most attention in the civilian field. In Fig. 11 is shown a representative data set acquired with the JPL/NASA ATI system at the Strait of

Messina, Italy, in 199110. The three images show radar intensity, across-track velocity, and decorrelation time.. The data were acquired at a flight track heading of 190° and the incidence angle vanes from 20° in the near range to 60° in the far range. The data have been corrected for motion caused by aircraft turbulence, and the accuracy of this correction is seen from the solid blue color of land areas indicating zero velocity. The interferometric velocity in the strait is 1.1 m/see towards the radar corresponding to a ground projected 2 m/sec south going current, which is to be compared to a value of 2.1 m/sec from local tide tables. Note that the velocity slightly south of the strait has been wrapped around the color wheel and the yellow color surrounded by purple thus corresponds to a slant range velocity of -1.6 m/see equivalent to a ground range velocity of 2.3 m/see away from the radar. This example demonstrates the ability of an along-track interferometric SAR system to provide a spatial map of currents. The correlation time image further enhances chaotic behavior such as "tagli" (similar to tidal bores), upwelling and different ocean regions as features with decreased coherence time.

Single baseline interferograms collected with the a previous JPL system has also provided currents and wave spectra, which very closely resembled those derived from in situ measurements [Goldstein et al., 1989; Marom et al., 1990].

Other potential radar velocity mapping applications include in the civilian domain measurements of the velocity of drifting sea ice. Military applications include the detection of moving targets, [Shnitkin, 1994]. The utilization of the U.S. J–STARS (Joint Surveillance Attack Radar System) as a long range system providing land surface maps and detection of moving targets, was generally hailed as one of the major technological successes of the Gulf War in 1991.

---

10 Fig. 11 and the data evaluation is from [Carande, 1994]

4 Change Mapping

4.1 Theory and Algorithms

By combining complex radar images acquired on nearly identical tracks, one has a measurement situation quite similar to the velocity mapping already discussed. The main differences are firstly, that the time lag is much larger, typically days to years for satellite observations and tens of minutes to hours for aircraft acquisitions, and secondly that there is often a significant spatial baseline component present. Occasionally, however, satellite orbits will repeat so accurately so that the baseline is only a few meters in which case corrections for the topography is not required at all, this was for instance the case for the glacier studies by Goldstein et al., [1993].

In this section we derive the equations needed for calculating ground displacement fields from interferometric synthetic aperture radar measurements in the case where both topographic phase contributions and displacement effects are important (based on a derivation given in [Zebker et al., 1994b]). We first recall the case where no ground movement between radar observations occurs, Neglecting the term of order $(\delta\rho)^2$ in equation (5) we obtain,

$$\begin{aligned}\delta\rho = \rho_2 - \rho_1 &= -\frac{2\rho_1 B}{(\rho_1+\rho_2)}\sin(\theta-\alpha)+\frac{B^2}{(\rho_1+\rho_2)} \\ &\cong -B\sin(\theta-\alpha)+\frac{B^2}{2\rho_1}\end{aligned} \tag{31}$$

For simplicity in describing the basic principles, we will ignore the second term on the right-hand side, although it is not necessary for the. analysis presented below. In the case of spaceborne geometries the second term on the right hand sideof(31) typically represents an overall bias of less than 1 cm, The approximation we use. in the following is

$$\delta\rho \cong -B\sin(\theta - \alpha) \\ = -B_{\parallel} \tag{32}$$

where $B_{\parallel} \cong B\sin(\theta - a)$ is the component of the baseline parallel to the look direction, Equations (2) and (32) show that the measured phase of an interferometer is the component of the interferometer baseline parallel to the look direction to a given point on the surface measured in wavelengths, where for the repeat pass situation $p = 2$ in equation (2). The height sensitivity of the instrument was previously discussed in section 2.1,

If a second (denoted prime) interferogram is acquired over the same area, sharing one orbit with the previous pair so that ρ and θ are unchanged, we can compare the interferogram phase-s with each other. This second interferogram is acquired with a different baseline B', and baseline orientation *a'*, thus a different B' $_{\parallel}$. Combining the two measurements we get,

$$\frac{\phi'}{\phi} = \frac{B'_{\parallel}}{B_{\parallel}} \tag{33}$$

In other words the ratio of the phases is equal to the ratio of the parallel components of the baseline,

Now consider the situation of two interferograms acquired over the same region as before but in this case a surface process (e.g. an earthquake) has displaced each resolution element between observations for the primed interferogram. The displacements are assumed highly correlated within a resolution cell so that the radar echoes remain correlated. Here in addition to the phase dependence on topography there is a phase change due to the radar line-of-sight component of the displacement Ap. In this interferogram the phase ϕ' will be given by

$$\phi' = \frac{4\pi}{\lambda}\left(B'_{\parallel} - \Delta\rho\right) \tag{34}$$

The displacement term Ap adds to the topographic phase term. If the data from the initial unprimed interferogram are scaled by the ratio of the parallel components of the baseline and

subtracted from the primed interferogram, we can obtain a solution dependent only on the displacement of the surface, as follows

$$\phi' - \phi \frac{B'_{\parallel}}{B_{\parallel}} = -\frac{4\pi}{\lambda} \Delta\rho \tag{35}$$

Since the quantity on the left is determined entirely by the phases of the interferograms, scene topography (which is determined by the interferometric pair acquired with no surface displacement in between), and the orbit geometries; the line of sight component of the displacement $\Delta\rho$ is measurable for each point in the scene,

The ratio

$$\frac{B'_{\parallel}}{B_{\parallel}} \frac{\sin(\theta - a')}{\sin(\theta - \alpha)} \tag{36}$$

is a function of the angle θ, which depends both on the illumination geometry and also the topography at each point in the radar image. To evaluate (35) via (36) directly, one must solve for the topographic map of the area of interest from the interferometric data or obtain the elevation data from another source. This involves, as discussed earlier, unwrapping the phase and determining the absolute phase.

An indirect approach presented in [Zebker et al., 1994b] demonstrates the basic concept of displacement mapping but does not require the step of either topographic solution or registration of dissimilar data sets (such as a radar interferogram and an independent DEM). We will proceed with this approach in the following.

First a term that would exist *even* in the absence of topography on a spherical earth is removed The phase corrected for the "curved Earth" effect, denoted ϕ_{flat}, is given by

$$\phi_{flat} = -\frac{4\pi}{\lambda} B(\sin(\theta - \alpha) - \sin(\theta_0 - a)) \tag{3'7}$$

where θ_0 is the look angle to each point in the image assuming a constant local reference height, The interferogram phase after this correction represents the distortion of the interference grating pattern due to topographic variation relative to the spherical reference surface and displacements due to motion in the scene.

Noting that the deviation of the exact θ from θ_0 is small[11], we can expand the first term on the right hand side of (37), leading to

$$\phi_{flat} = -\frac{4\pi}{\lambda} B \cos(\theta_0 - \alpha)\,\delta\theta \tag{38}$$

where $\delta\theta = \theta - 0_0$. Numerically, ϕ_{flat} is equal to the product of the perpendicular component of the baseline $B_\perp$, assuming no topography is present on the surface, and the topographic angular distortion $\delta\theta$. Thus, the ratio $\phi_{flat} / \phi'_{flat}$ is now in terms of θ_0 rather than O, and depends only on the viewing geometry and the baseline. If we now restate the differential phase equation (35) above in terms of the flattened phase ϕ_{flat}, we obtain

$$\phi'_{flat} - \phi_{flat} \frac{B' \cos(\theta_0 - a')}{B \cos(\theta_0 - a)} = \quad - \sim \quad \Delta\rho \tag{39}$$

With this function, we can now solve directly for the displacement $\Delta\rho$ without requiring the exact values of O, and hence the topographic information, at an intermediate step.

Note that if the baseline used in the flattening operation (equation 37 above) is not exactly the true baseline value, equation (38) will contain error terms and the subsequent displacement maps will be distorted

---

[11] This approximation is excellent for spaceborne system. It should be used with care if aircraft data are being processed.

The phase in radar interferograms thus depends both on the local topography and also on any motion that may occur between viewing instances, We may compare the sensitivity of the phase measurement to the phenomena of topography and displacement, which may be derived by differentiating (39) with respect to height through $B_{\perp}$ and $\Delta\rho$. In the former case, we find

$$\frac{\partial\phi'}{\partial\theta} \approx \frac{4\pi}{\lambda} B' \cos(\theta - \alpha') \tag{40}$$

and, using $\partial h = p \sin\theta\, \partial\theta$, obtained from equation (7)

$$\frac{\partial\phi'}{\partial h} \approx \frac{4\pi}{\lambda} \frac{B' \cos(\theta - \alpha')}{p \sin\theta} \tag{41}$$

For the displacement case we have

$$\delta = \frac{4\pi}{\lambda} \tag{42}$$

Since the distance p typically is very much greater than the baseline distance B, it is evident from equations (41 and 42) that the phase is much more sensitive to surface changes than to topography. Thus, while radar interferometry can be used to measure topography to an accuracy of meters, displacements may be determined to the centimeter or millimeter level,

This ratio of sensitivities illustrates the power of the interferometric technique to detect small surface movements or deformations.

There are, however, two very important limitations to the interferometric technique. First, radar echoes acquired on the three passes must correlate with each other-- this is the issue of temporal decorrelation which we have discussed earlier.

The second limitation, more important for this study, is that the phases must be "unwrapped" before data from one interferogram maybe used to correct the second interferogram to estimate the displacement phases.

A second situation which can be resolved using similar techniques is when the displacement is not instantaneous, but rather a continuos movement over the observation time. This could for instance be the case when aircraft passes over glaciers are repeated several times per hour. In this case we have for both baselines,

$$\begin{aligned}\phi &= \frac{4\pi}{\lambda}\left(B\sin(\theta-\alpha)-ut\right)\\ \phi' &= \frac{4\pi}{\lambda}\left(B'\sin(\theta-\alpha')-ut'\right)\end{aligned} \tag{43}$$

where for each pixel the unknowns are θ and u. Applying the same flat Earth approximation which leads to equation (38) we get

$$\begin{aligned}\frac{\lambda}{4\pi}\phi_{flat} &\cong \delta\theta\, B\cos(\theta_0-\alpha)-ut\\ \frac{\lambda}{4\pi}\phi'_{flat} &\cong \delta\theta\, B'\cos(\theta_0-\alpha')-ut'\end{aligned} \tag{44}$$

which are two tines equations with two unknown, thus the topographic phase component and the velocity phase component are given as simple linear combinations of the two original interferograms.

4.2 Systems for change mapping

Any aircraft SAR can in principle be used for interferometric change mapping, however, navigation uncertainties are often on the order of severat hundreds of meters which means that baselines are unacceptably large and usually tracks are not sufficiently parallel: change mapping thus requires an unreasonable number of data takes to obtain a sufficient number of passes with useful acquisition geometries. Operating the CCRS SAR system, Gray and Farris-Manning [1993] used DME navigational data to repeat tracks in a area near Ottawa achieving baseline ranging from a few meters to more than a hundred meters. The Electromagnetic Institute of the Technical

University of Denmark is flying a fully polarimetric C-band SAR (EMISAR) on a Gulfstream G-3 of the Royal Danish Air Force, which has been enhanced with an aircraft track control system which is directly aimed at interferometric change detection applications. The radar system has access to a P-code GPS system available onboard which provides the radar with accurate knowledge of the aircraft position and can furthermore steer the aircraft via the aircraft's instrument landing system (ILS). The radar compares the position and the velocity measured by the GPS with the desired track parameters and calculates the position and velocity deviations in the up-down and right-left directions. These measurements are then used to emulate localizer (LOC) and glide slope (GS) signals for one of the aircraft's ILS systems. This track control system has now been flown for several month and the preliminary indications are that the aircraft position can be controlled to less than a meter off-set from the navigation reference, which in the case of P-code GPS is specified at 15 m. The accuracy in trying to repeat tracks within a few hours is, however, much better as several dominating GPS errors (e.g. ionospheric delay) shows up as common mode errors. The experience with the system is that the baselines obtained are within a couple of meters of the desired baselines, The system has so far acquired change detection data over drifting sand dunes (Fig. 12) and glacier ice.

The satellite systems which can and have been used for change mapping are the same as those already discussed in section 2.3,2. It is noted that with the planned launch of ERS-2, ESA is considering to put the ERS-1 and ERS--2 satellites in a tandem orbit configuration, with one satellite repeating the orbit of the other with a one day delay. In case this tandem configuration is implemented it would vastly increase the amounts of usable interferometry data for topographic applications as well as for change detection.

4.3 Applications for radar change mapping data

Change mapping is important in many areas. Monitoring natural disasters such as earthquakes, fires, flooding, or volcanoes is one type of application. There is an advantage in being able to predict the magnitude of the disaster at the earliest possible time, to monitor the situation as it unfolds, to assist in providing disaster relief, and finally to assess damage. Climate and Earth science studies are other areas where change mapping is important. It is for instance believed that alpine glaciers can act as early indicators of climate change. Also, the cartographic community is in constant need of updating maps which becomes stale at a seemingly ever increasing rate; urban development for instance calls for very frequent map updates. In this section we will discuss two applications where radar interferometry already has demonstrated its capability provide spatial change maps,

4.3.1 Earthquake monitoring

It is well documented that radar interferometry ean be used to map the coseismic displacement of earthquake, [Massonnet et al., 19931, [Massonnet et al., 19941, [Zebker et al., 1994b]. The magnitude 7.3 Landers earthquake of June 28 1992, approximately 150 km east of Los Angeles, took place in an area which had previously been covered by the ERS-1 SAR system. By combining data acquired before and after the earthquake it was thus possible to generate maps of the displacements in the line-of-sight direction.

Massonnet et al., [1993], applied a technique which required only two radar images. They derived a simulated interferometric phase due to topography from the orbit geometry and an available USGS DEM. essentially calculating, ϕ, as ϕ' of (34) assuming $\Delta\rho$ is zero thus making (35) a trivial subtraction. This approach only requires two complex SAR images, and automatic phase unwrapping techniques are not required, However, an existing DEM of the area

must exist and the accuracy of this approach will depend on the accuracy of the DEM and the baseline of the two passes. Also, when phase unwrapping is not applied one must manually count the number of fringes (properly considering increasing and decreasing phase cycles] from a reference point of known displacement, a tedious procedure at best. Massonnet et al, demonstrated using this approach that the displacement field of the Landers earthquake was in good agreement with the slip measured in the field, and the results of an elastic dislocation model, They also used this technique to image the line-of-sight displacement which occurred in the year following the main shock, [Massonnet et al., 1994].

Zebker et al. [1994b] used a technique which is basically identical to what was outlined in section 4.2. This technique relies on 3 complex SAR images, one acquired before the main earthquake, two after. The data sets acquired after the earthquake [2] are combined to provide the topographic phase, ϕ, an interferogram formed from data acquired on both sides of the earthquake provides, #. The displacement $\Delta\rho$ is then obtained from equation (35). This approach does not require an existing DEM, however, it does require 3 SAR images, and it does require that the interferograrns are phase unwrapped. This on the other hand has the important benefit that the absolute value of the displacement is estimated, thus alleviating the need for manually counting fringes. Zebker et al. presented a map with contour lines of the radar line-of-sight motion, and compared those results to GPS field measurements. The area of overlap between the field survey and the radar displacement image contained 18 points of known displacement from GPS and

---

12 Ideally the two images used to derive the topographic component should have no displacements in between acquisitions which suggest that they should have a small time baseline and/or be acquired before any earthquake displacements occur.

trilateration measurements and the rms displacement difference was 19 cm (the rms of the GPS displacement measurements of the 18 reference points was 68 cm).

Similar techniques have been applied by Gilles Peltzer and Paul Rosen of JPL to analyze the Eureka Valley magnitude 6,1 earthquake, May 17, 1993 (see Fig. 13). This figure shows the displacement map derived from ERS-1 data acquired on November 14 and 23, 1992, and November 8, 1993. An ellipsoidal depression of approximately 15 cm caused by the earthquake is clearly visible.

4.3,2 Glacier velocity mapping

Glacier dynamics are, as already mentioned, important observable in global climate studies, Important parameters are ftow velocities, changes in glacier topography, determination of terminus as well as the grounding-line. Glacier dynamics monitoring can also be accomplished by applying interferometric SAR techniques, Goldstein et al. [1993] used this technique to generate a flow image of the Rutford Ice Stream in Antarctica (Fig. 14). Due to orbital convergence it is much more likely to find interferometric pairs with small baselines close to the poles. Goldstein et al. based their analysis on passes which were so close (4 m) that the sensitivity to topography was nearly zero[13]. Thus they avoided problems with the topographic component completely. They were able to use the interferometric data to accurately delineate the grounding-line. They converted the measured line-of-sight measurements to horizontal velocities and measured a flow velocity of 390 m per year which is in good agreement with surface based measurements. It is in that context interesting to note that down stream from the grounding line there are significant tidal effects

[13] From equation (45) the height sensitivity for a 4 m baseline using ERS-1 parameter can be bound to 2.7 mrad per m, or 2.35 km per fringe.

(vertical velocities) which gives rise to instantaneous velocities in the line-of-sight direction which are much larger than the horizontal flow velocities of interest. Thus it is of primary importance to correct for such effects if interferometric measurements are to be used on the floating part of the glacier.

The situation where both the spatial and the temporal baselines are significant has not been addressed so far to our knowledge, It is a particularly difficult situation as the glacier motion is most likely not smooth, in which case the equations presented in equations (43) and (44) would not apply either. To measure the glacier motion while also correcting for topography, it would therefore be important to find data sets with baselines having widely different sensitivities to displacements and topography.

The interferometric measurement of "nearly" instantaneous glacier velocities will be an important contribution to studies of glaciers as velocities which can be measured today are generally average velocities over fairly long observation times (e.g. one year).

5 Future Developments

Interferometric techniques to produce topographic maps, velocity maps, and monitor change detection are moving beyond the demonstration stage. It will be expected of future topographic systems, whether airborne or spaceborne, that they provide calibrated data, including absolute locations referenced to a well defined datum (e.g. WGS–84). Processing systems being developed are already fully automatic up to the DEM formation stage, and future systems will incorporate automated mosaicking and feature recognition capabilities.

It can be expected that information in the interferometric data will be utilized in new ways, for urban applications, for automated mapping etc. Multiple baseline and multiple frequency systems will also allow studies of volume targets (forest) and media with low loss (ice caps and glaciers). It is also likely that other combinations of multiple baselines, such as simultaneous time- and space-baselines on one platform will provide new insight into dynamic phenomena, such as ocean currents and wavespectra.

5.1 Emerging Applications

Urban applications of interferometric data are both challenging and potentially very rewarding. Urban mapping typically requires high resolution, but is also difficult as the nature of man made targets, with vertical walls causing lay-over and shadowing, artificial corner reflectors, a large dynamic range and multi-path, makes the urban scene prone to phase unwrapping errors and other practical problems. However, an urban area is a dynamic environment which requires frequent map up-dates. The special problems in this field are already being addressed today.

An important next step is the development of automated mapping algorithms which will process the "raw" topographic data, and the associated radar imagery, to extract features and generate a map product in a standard mapping format in digital form.

An interesting measurement problem relates to measuring layered media. When generating a topographic map of a forest area, one would like to know whether the height provided is the one of the top of the trees or the level of the bottom of the forest. The answer will depend on the wavelength applied as longer wavelengths generally penetrate further. It would of course be desirable to measure both, but if that is not possible it is important to know what was measured. By applying multiple frequency interferometric systems it will be possible to measure different layers and obtain at least some of this information. Another technique being studied (personal communication, E. Rodriguez, JPL) is to use the interferometric decorrelation, appropriately corrected for SNR effects and spatial baseline decorrelation, to measure volumetric scattering. This could provide the effective penetration depth of a given target which would be an important parameter in addition to the measured elevation. Yet another multi-channel technique which will likely be studied in the near future is to decompose polarimetric radar observations and form interferometric products from the different decomposition components. Since the different components of the decomposition are theoretically generated by different scattering mechanisms it may be possible to measure the height of the transition from ground to tree trunks separately from the height of the crown,

The measurement techniques developed to date to estimate ocean currents are under certain conditions ambiguous as both phase and group velocities of the wave spectrum can contribute to the measured interferometric velocity, Multi-baseline and/or multi-frequency interferometers is also expected to help removing such ambiguities.

5.2 Aircraft Systems

As indicated above a dual-frequency topographic interferometer is a significant priority scientifically [14]. At JPL an L-band addition to the existing TOPSAR will allow investigations of the frequency dependence of digital topography acquired from such a system by comparing data acquired at L and C band. The multifrequency studies will be of particular use in understanding, for example, the bias of an interferometric radar topographic instrument when used over vegetated areas. This is an important problem for future satellite missions, as the frequency of operation cannot be chosen without the characterization of this phenomenon. The expected performance of the L-band system is similar to the existing C-band system. The goal is to produce DEMs with a height accuracy better than 2 m, requiring no tie point knowledge, precisely co-registered at the two frequencies. This capability follows from operating the L and C band systems simultaneously, and processing the raw data in an integrated manner.

Comparing the results at the two frequencies will lead not only to improved height maps of the areas but could in principle permit estimation of biogeophysical factors,

A second interesting development is the precise aircraft track-control capability mentioned earlier in section 4.2. Systems like the EMISAR system will allow accurate design of the baselines required for a particular experiment. For glacier dynamics studies it is possible to repeat tracks with virtually zero baseline, at time baselines ranging from tens of minutes to hours, days and years. With the advent of kinematic GPS technology for dynamic platforms it will be possible to obtain navigation accuracies in the submeter range even in remote areas.

---

[14] The JPL along-track interferometer is as mentioned earlier already a dual frequency (L/C) system.

5.3 Spaceborne Systems

Global topographic mapping probably requires satellite instrumentation, and various configurations have been proposed to produce these data. In fact NASA has been studying such a mission for several years to support many ongoing research programs and the general science community. Consideration of accuracy, facility of data reduction, and cost has led to the selection of the interferometric radar technique as the leading candidate for this mission, The principal goal of this mission is to map the topography of the entire Earth in less than a year at an accuracy similar to that exhibited by 1:50000 maps.

Two possible spacecraft implementations are presented in this section. Each approach has its own limitations based on available technology. Thus, many of the limits to performance described here result from details of the implementation rather than by shortcomings of the technique.

If we eliminate repeat pass implementations as unreliable for a global mapping mission requiring contiguous, uniform data over much of the Earth, two alternatives for interferometric radar instrument designs remain: i) a single spacecraft with two displaced antennas, and ii) two spacecraft, each with a synthetic aperture radar, flying in formation to form the interferometer baseline. For each system, the basic limitations to interferometer performance as described above remain. Signal to noise ratio must be maximized in the constrained spacecraft environment, the baseline must be of sufficient length to give the desired height sensitivity without causing too much baseline decorrelation, and the baseline attitude must be measured at the 1 arc second level.

The single spacecraft approach would achieve the required baseline lengths by mounting one or troth of the antennas on a boom at a distance from the spacecraft. A boom would likely be limited to about 25 m length, therefore to form an adequate baseline the wavelength would have to be short, preferably 2 cm (Ku-band) or less, The effective boom length, however, ean be doubled by "ping-ponging," or alternately transmitting from each antenna as described previously, at a cost of

cutting pulse repetition rate and the average power per channel by a factor of two, which also increases azimuth ambiguities due to undersampling of the Doppler spectrum.

Baseline attitude determination would be achieved by measuring both the rigid body spacecraft attitude and the structural distortion between the two antennas. The spacecraft attitude can be measured by a star tracking system and the structural distortion by a laser metrology system, Of these two the measurement of spacecraft attitude to less than one are-second is the more difficult. Current star trackers cannot measure absolute attitude to less than several are-seconds, due to limitations in the trackers themselves, uncertainties in mechanical spacecraft flexure, and by limitations in absolute knowledge of star positions.

Several of the above limitations could be reduced by using two spacecraft to form the interferometer by flying in proper formation. Since the baseline can be much longer, a twin spacecraft approach could utilize a much lower frequency, and hence technologically simpler, radar system (see L–band option in tables 4 and 5). Such a system could utilize L-band with a wavelength of 24 cm as a nominal approach due to the relative technological maturity of the radar electronics -SEAS AT, SIR-A, SIR-B, SIR-C, and the Japanese JERS - 1 satellites all have L-band radar channels. Here one would navigate the two spacecraft in "parallel" orbits, identical except in node crossing, to form any desired baseline length, The baseline attitude knowledge requirement is still at the 1 arc-second level, but differential Global Positioning Satellite (GPS) techniques promise to determine the relative positions of the spacecraft to a precision of about 3 mm in all directions [Bertiger, 1994]. If the baseline length is nominally 1000 m, this translates to 0.62 second of are, well within the requirements.

A complete error budget for both implementations is shown in table 6.

6 References

[Bert.iger 1994] Bertiger, W.I. et al.,GPS Precise Tracking of TOPEX/Poseidon: Results and Implications, submitted to J. Geophys. Res. TOPEX/Poseidon Special Issue, Nov. 1993.

[Carande, 1994] Carande, R. E., "Estimating ocean coherence time using dual-baseline interferometric synthetic aperture radar", IEEE trans Geoscience and Remote Vol.32, No.4, pp 846–854, July 1994

[Curlander and McDonough, 1991] Curlander J. and R.N. McDonough,"Synthetic Aperture Radar, Systems and Signal Processing", John Wiley & Sons, Inc.

[ERIM, 1994] ERIM, IFSARE paper

[Evans et al., 1992] Evans, D. L,., T.G. Farr, H.A. Zebker, J.J. van Zyl, and P.J. Mouginis-Mark, "Radar Interferometry Studies of the Earth's Topography", Eos, trans American Geophysical Union, Vol.73, No.52, Dec. 29, 1992

[Farr et al. , 199X] EOS paper ref

[Fullman et al., 1994] Fullman, H., H, Holt, J. O'Brien, and L. Orwig, "Accuracy validation of the IFSARE radar", Natl. Aerospace and Electronics Conference, May 24, 1994

[Gabriel et al., 1989] Gabriel, A. K., R. M. Goldstein, and H.A. Zebker, "Mapping small elevation changes over large areas: differential radar interferometry", J.Geophysical Research, Vol. 94, no. B7, pp 9183-9191, July 10, 1989

[Gatelli et al., 1994] Gatelli, F., A. Monti Guarnieri, F. Parizzi, P. Pasquali, C. Prati, and F, Rocca, "Use of the spectral shift in SAR interferometry: applications to ERS–1", submitted to IEEE trans. Geoscience and Remote Sensing.

[Graham, 1974] Graham, L.C., "Synthetic interferometer radar for topographic mapping", Proc. IEEE", 1974, Vol. 62, pp 763-768

[Goldstein and Zebker, 1987] Goldstein, R, M., and H.A. Zebker, "Interferometric radar measurement of ocean surface currents", Nature, Vol. 328, No. 6132, pp. 707-709, 20 August 1987

[Goldstein et al., 1988] Goldstein, R, M., H.A. Zebker, and C.L. Werner, "Satellite radar interferometry: Two-dimensional phase unwrapping", Radio Science, July-August 1988, Vol. 23, No, 4, pp 713-720

[Goldstein et al., 1989] Goldstein, R. M., T.P. Barnett, and H.A. Zebker, "Remote sensing of ocean currents", Science, 8 December 1989, Vol. 246, pp. 1282-1285

[Goldstein et al., 1993] Goldstein, R.M., H. Engelhardt, B. Kamb, and R.M. Frolich, "Satellite radar interferometry for monitoring ice sheet motion: Application to an Antarctic ice stream", Science, 3 December 1993, Vol. 262, pp. 1525-1530

[Gray and Farris-Manning, 1993] Gray A.L. and P.J. Farris-Manning, "Repeat-pass interferometry with airborne synthetic aperture radar", grs, 1993, Vol. 31, no. 1, January, pp 180-191

[Griffin et al., 1993] Griffin, M. F., E.C. Boman, 1. Metal, and L. Orwig, "Estimating ocean-scene coherency-time with a multi-aperture radar", IEEE international Conference of Acoustics, Speech, and Signal Processing, April 27-30, 1993

[Li and Goldstein, 1990] Li, F. and R. M. Goldstein, "Studies of multi-baseline spaceborne interferometric synthetic aperture radars", grs, 1990, Vol. 28, no. 1, January, PP 88-97

[Madsen et al., 1993] Madsen, S.N., H.A. Zebker and J.M. Martin, "Topographic mapping using radar interferometry: Processing techniques", grs, 1993, Vol. 31, no. 1, January, pp 246-256

[Maron et al., 1990] Marom, M., R.M. Goldstein, E.B. Thornton, and L. Shemer, "Remote sensing of ocean wave spectra by interferometric synthetic aperture radar", Nature, 28 June 1990, Vol. 345, pp. 793-795

[Massonnet et al., 1993] Massonnet, D., M. Rossi, C. Carmona, F. Adragna, G. Peltzer, K. Feigi, and T. Rabaute, "The displacement field of the Landers earthquake mapped by radar interferometry", Nature, 8 July 1993, Vol. 364, pp. 138-142

[Massonnet et al., 1994] Massonnet, D., K. Feigi, M. Rossi, and F. Adragna, "Radar interferometric mapping of deformation in the year *after the* Landers earthquake", Nature, 19 May 1994, Vol. 369, pp. 227-230

[Rodriguez and Martin, 1992] Rodriguez, E., and J.M. Martin, "Theory and design of interferometric synthetic aperture radars", IEE Proceedings-F, Vol. 139, No, 2, April 1992, pp 147-159,

[Rodriguez et al., 1994] Rodriguez, E., D, Imel, and S.N. Madsen, "The accuracy of airborne interferometric SAR's", IEEE trans. Aerospace and Electronic Systems, Vol. 139, No. 2, April 1992, pp 147-159.

[Shnitkin, 1994] Shnitkin, H., "Joint STARS Phased Array Radar Antenna, IEEE proc. of the Antennas and Propagation Symposium, Seattle, WA, June 19, 1994

[TSWG, 1988] Topographiccience Working Group, "Report to the land processes branch, Earth science and applications division", NASA, 1988

[Zebker and Goldstein, 1986] Zebker, H. and R. Goldstein, "Topographic Mapping from Interferometric {SAR} Observations", jgr, 1986, Vol. 91, B5", pp 4993-4999

[Zebker and Villasenor, 1992] Zebker, H. A., and J,. Villasenor, "Decorrelation in interferometric radar echoes", grs, 1992, Vol. 30, no, 5, pp 246-256, September 1992

[Zebker et al., 1994a] Zebker, H. A., C. Werner, P.A. Rosen, and S. Hensley, "Accuracy of topographic maps derived from ERS-1 Interferometric radar", IEEE trans Geoscience and Remote Sensing, Vol. 32, No. 4, July 1994, pp 823-836.

[Zebker et al., 1994b] Zebker, H. A., P.A. Rosen, R. M. Goldstein, C. Werner, and A, Gabriel, "On the derivation of coseismic displacement fields using differential radar interferometry", in press JGR Earth.

Acknowledgment

The author would like to thank ...

The authors are with the Jet Propulsion Laboratory, California Institute of Technology,

Appendix

A.1 Transferring a measurement from one squint angle to another.

Often it is desirable to reference the processed SAR data to a squint angle which is different that of the acquisition, Such a transfer of reference impacts the range, the azimuth and the phase reference (this is a consequent of the range shift) The geometry is shown in figure A. 1.

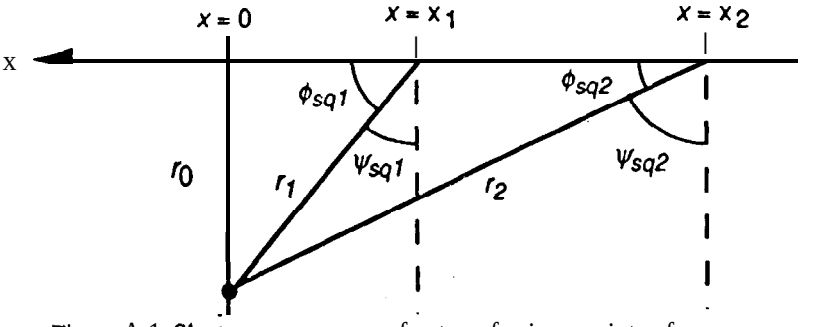

Figure A.1. Slant range geometry for transferring squint reference.

$$
\begin{aligned}
r_0 &= r_1 \sin \phi_{sq1} = r_2 \sin \phi_{sq2} \\
&= r_1 \cos \psi_{sq1} = r_2 \cos \psi_{sq2} \\
r_0 &= -x_1 \tan \phi_{sq1} = -x_2 \tan \phi_{sq2} \\
&= -x_1 \cot \psi_{sq1} = -x_2 \cot \psi_{sq2}
\end{aligned}
\qquad \text{(A1)}
$$

A.2 Spherical geometry, the (s, c, h) coordinate system.

A rectangular (x, y, z) = (along-track, across-track, height) coordinate system can be generalized to a spherical equivalent which we call the (s, c, h) system. The coordinates are defined as follows

$$
\begin{aligned}
x &= (R_a + h)\cos\phi_s \cos\phi_c \\
y &= (R_a + h)\sin\phi_s \cos\phi_c \\
z &= (R_a + h)\sin\phi_c \\
s &= R_a\phi_s \\
c &= R_a\phi_c
\end{aligned}
\tag{A.2}
$$

where R_a is the radii of curvature of the sphere approximating the Earth. The corresponding unit vectors are,

$$
\hat{s} = \begin{pmatrix} -\sin\phi_s \\ \cos\phi_s \\ 0 \end{pmatrix} \qquad \hat{c} = \begin{pmatrix} -\cos\phi_s \sin\phi_c \\ -\sin\phi_s \sin\phi_c \\ \cos\phi_c \end{pmatrix} \qquad \hat{h} = \begin{pmatrix} \cos\phi_s \cos\phi_c \\ \sin\phi_s \cos\phi_c \\ \sin\phi_c \end{pmatrix} \tag{A.3}
$$

Note that if the original platform positions are given in an (x, y, z)org system (such as for instance WGS-84) which is not aligned with the along-track, across-track, and height directions then a transformation (rotation and off-set) from that system to an intermediate (x, y, z)sch system is required. The (x, y, z)sch system (which is the one used in equations (A.2) and (A.3)) must be aligned such that it has its ongin at the center of the approximating sphere and such that the radar track is basically in the x-y plane.

Figures

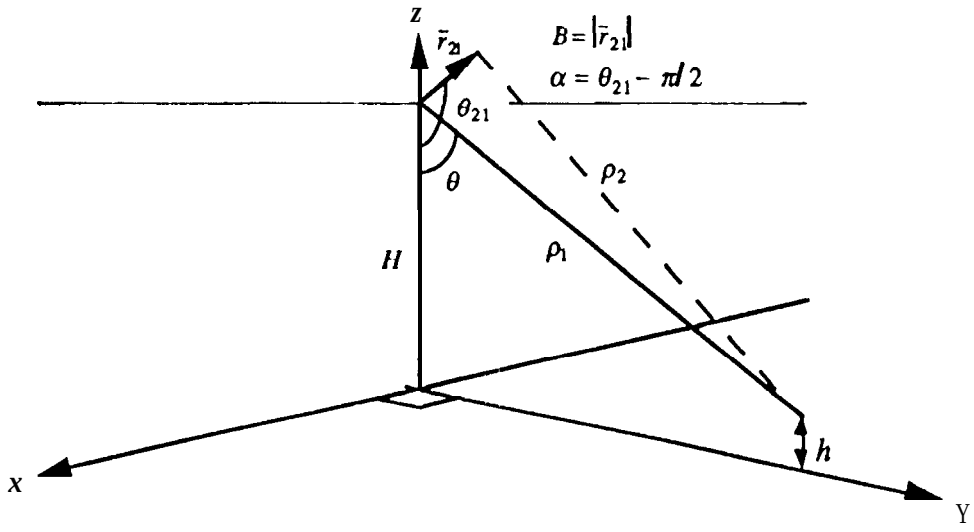

Fig.1 Across-track interferometer geometry. Platform is flying parallel to the x-axis at an elevation of H. Note use of the angle $a = \theta_{21} - \pi / 2$, the baseline angle relative to horizontal.

Fig.2 A topographic data set of the Ft. Irwin area in Southern California, collected with the JPL/NASA TOPSAR system.

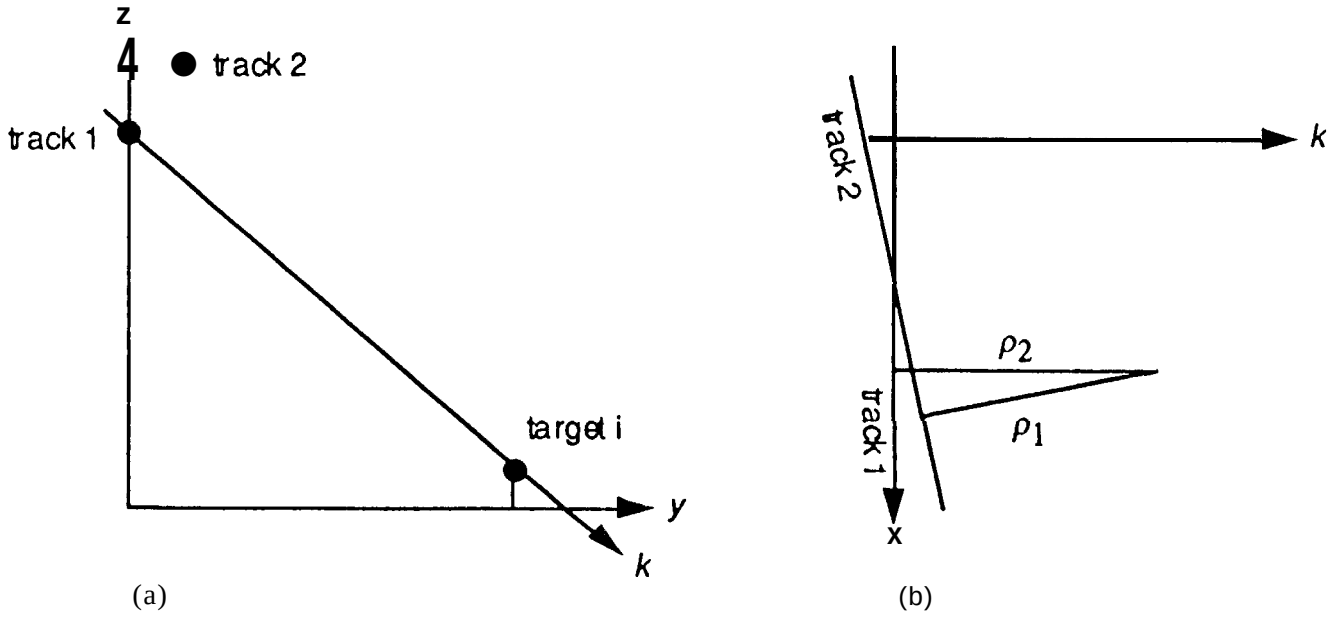

(a) (b)

Fig, 3, Slant range plane, k, as viewed (a) looking into track 1, (b) seen from above,

Fig, 4. Perspective view generated from ERS–1 data acquired over a region in the Mojave Desert in California which includes the Pisgah lava flow, visible near the scene center.

Fig. 5. Correlation plotted versus time (from Zebker and Villasenor, [1992])

Fig. 6. Average correlation for ERS- 1 data, Correlation in 6a (with a six day baseline) is considerable higher than 6b (with a three day baseline)

Fig. 7. TOPSAR generated digital elevation model of the Galapagos Islands (mosaic by Scott Hensley, JPL)

Fig. 8. Perspective view of an unnamed glacier on Bylot Island, NWT, Canada. Scene generated from geo-coded interferometric SAR data flown by the Canada Centre for Remote Sensing (courtesy Lawrence Gray, CCRS)

Figure 9 User requirements for topographic mapping

Fig. 10. Height error map, for test area in Ft. Irwin, California

Fig. 11 a), the top image shows the SAR intensity image at L-band. Ttre aircraft is flying right to left and the near range is at the top of the image; b) a color coded version of the interferogram formed from the FF and AA channels; c) a correlation image as generated using equation (30).

Fig. 12 Perspective view of Sand dunes in northern Jutland, Denmark. Data acquired in repeat track mode by the Electromagnetic Institute, Technical University of Denmark, Statistical height error approximately 10 cm.

Fig. 13 Image of 15 cm elliptical depression in the Eureka Valley generated by a May 17, 1993, magnitude 6.1 earthquake (courtesy Gilles Peltzer and Paul Rosen, JPL).

Fig. 14 Radar interferogram of part of the Rutford Ice Stream, Antarctica, This interferogram was used to determine the grounding line, and measure the glacier velocity, [Goldstein et al., 1993].

List of Tables

TABLE 1. SINGLE PASS AIRBORNE SYSTEMS

Radar parameter	*JPL-TOPSAR*	*CCRS-INSAR*
Frequency	5.3 GHz	5.3 GHz
Range bandwidth	40 MHz	30 MHz
Peak transmit *power*	1000W	16 kW
Antenna azimuth beam width	2°	3.1°
Antenna elevation beam width	30°	30°
Baseline length	2.5 m	2.8 m
Baseline angle rel. horizontal	62.8°	49.4”
Ground velocity	210 m	130 m
Operating altitude	approx. 9 km	approx. 6.4 km
Look angles	30-55”	30–55°
Slant range swath	10km	8 km
Processed ground range swath	12.8 km	10.5 km

TABLE 2.

TWO-PASS INTERFEROMETRY, SATELLITE SYSTEMS

Radar parameter	*SEA SAT*	*ERS-1*	*JERS-1*
Frequency	1.275 GHz	5.3 GHz	1.275 GHz
Range bandwidth	19 MHz	15.55 MHz	15 MHz
Peak transmit power	1000W	4800 W	11 OO-15OOW
Pulse repetition rate	1463-1647	1679 nominal	1505-1606
Antenna dimensions	10.7 by 2,16 m	11 by 1 m	12 by 2.2 m
Antenna elevation beam width	6,2°	6°	6.2°
Critical baseline length	4500 m	1115 m	4500 m
Altitude decay, appt.	10 m/day	10 m/day	10 m/day
Satellite altitude	800 km	790 km	568 km
Look angles	20–26°	21–26°	35”
Ground range swath ,	100 km	100 km	85 km

TABLE 3. AIRSAR ATI MODE SYSTEM PARAMETERS

Radar parameter	*JPL–ATI L-band*	*JPL–ATI C-band*
Frequency	1.25 GHz	5.3 GHz
Range bandwidth	20 or 40 MHz	20 or 40 MHz
Peak transmit power	6000 W	1000 w
Antenna length	1,36 m	1.6m
Antenna elevation beam width	44°	50°
Baseline length	19.8 m	1.9 m
Polarization	HH or VV	HH or VV
Channels	FF, FA, AF, AA	FF, FA, AF, AA
Nominal lag times	47 and 94 msec	4.5 and 9.0 msec
Operating altitude	approx. 9 km	approx. 9 km

TABLE 4. SPACEBORNE INTERFEROMETRIC KU- AND L-BAND RADAR SYSTEM

Parameter	*Ku-find*	*L-band*
Wavelength, m	0.02	0.24
Peak power, watts	750	1600
Pulse rate, Hz	3800	2100
Pulse length, μ sec	60	50
Antenna length, m	5	9
Antenna width, m	0.65	3.5
Antenna gain, dB	49.9	38.4
Range bandwidth, MHz	20	20
Receiver noise temperature, K	700	600
Antenna baseline, m	2s	800-2000 (variable)
Baseline angle (α), deg	30	0
Slant range resolution, m	7.5	7.5
Azimuth resolution, m	3.3	5.9
Orbit altitude, km	440	564
Look angle, deg	30	30
Orbit repeat interval, days	241	84

TABLE 5. COMPARATIVE DESIGN CONTROL TABLES

Parameter	*Ku-band*	*L-band*
	(dB/dBW)	(dB/dBW)
Peak power	28,8	32.0
Antenna directional gain	49.9	38.4
Antenna efficiency	-3	-3
$1\over 4 \pi$	-11	-11
$1\over R^2$	-114.1	-116.3
Illuminated area	75,8	84.2
σ^0	-13	-20
$1\over 4 \pi$	-11	-11
$1\over R^2$	-114,1	-116.3
Antenna area	5.3	15
Antenna efficiency	-3	-3
System losses	-3	-3
Oversampling gain	2.1	2.1
Total	-110.3	-111.9
Thermal noise (k'IIt)	-125.2	-126.9
Signal to noise ratio	14.8	15.0

TABLE 6. ERROR BUDGETS (ALL VALUES IN METERS)

Parameter	*Ku-band*		*L-band*	
	Flat terrain	Sloped terrain	Flat terrain	Sloped terrain
Height errors, m				
Phase noise error	3.26	5.32	1.94	1,17
Baseline error	0.00	0,00	0.71	1.15
Attitude error	1.23	2,01	0.98	1.59
Orbit height error	0.10	0,10	0.10	0.10
Other	0.10	0.16	0.10	0.16
RSS total	3.48	5.68	2,29	3.73
Across-track position errors, m				
Phase noise error	5,65		3,36	
Baseline error	0.00		1.22	
Attitude error	2,13		1.69	
Navigation error	3.00		3.00	
Other	0.10		0.10	
RSS total	6.74		4.97	
Along-track position errors, m				
Orbit timing error	0.01		0.01	
Navigation error	3.00		3.00	